ACS APPLIED MATERIALS & INTERFACES

Research Article

www.acsami.org

Vertically Oriented Iron Oxide Films Produced by Hydrothermal Process: Effect of Thermal Treatment on the Physical Chemical Properties

Lucas C. C. Ferraz, Waldemir M. Carvalho, Jr., Denise Criado, and Flavio L. Souza*

Centro de Ciências Naturais e Humanas, Universidade Federal do ABC, 09210-170, Santo André, SP, Brazil

Supporting Information

ABSTRACT: Our study describes the influence of the thermal treatment on the fundamental properties of the vertical oriented iron oxide nanorods synthesized under hydrothermal condition onto a conductor substrate. X-ray diffraction and X-ray absorption near edge structure spectra were used to investigate the phase evolution from iron oxyhydroxide (β-FeOOH) to pure hematite phase. The formation of nanorods distributed along of substrate was observed by top-view SEM images and the rod growth preferentially oriented at the highly conductive (001) basal plane of hematite, perpendicular to the substrate. Light absorption capacity increases with the temperature of treatment and the electronic transitions (direct and indirect electronic transition) were estimated from this result. From the electrochemical measurement, the hematite/electrolyte interface was evaluated. These findings demonstrated that the temperature plays an important role on the hematite (structural, morphological, and catalytic) properties and that many influences must work in great harmony in order to produce a promising hematite photoanode.

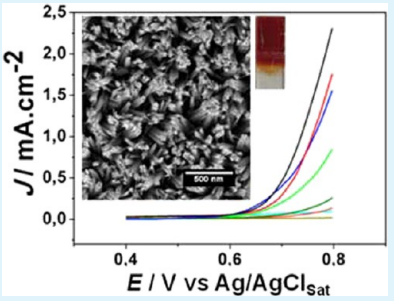

KEYWORDS: *iron oxide, 1D nanostructure, XANES, water oxidation, thermal treatment, hydrothermal process*

INTRODUCTION

Finding an alternative source of energy environmentally sustainable to supply the global demand is one of the most important challenges of the last decades. Among them, solar light provides a natural and inexhaustible source of energy. The solar energy can be explored simulating artificially the photosynthesis using nanostructured semiconductors to split water into hydrogen (H_2) and oxygen (O_2), resulting in a clean and renewable energy.[1−7] To make this pathway for artificial photosynthesis economically viable, a stable and efficient semiconductor to direct split water at its surface needs to be developed. Since the pioneering work done by J. J. P. Boddy[8] and A. Fujishima[9] using TiO_2, a large effort has been dedicated to find a material that satisfy all important requirements for actuate efficiently as a solar photoanode.[10] TiO_2 is one of the most studied semiconductors for that application, fulfilling most requirements, such as high chemical stability and favorable conduction band position; however, its overall efficiency to convert solar energy into hydrogen is low because of unfavorable band gap (around 3.2 eV) which permit only 5% of the solar irradiation to be absorbed.[11−18] Nowadays, the hematite (α-Fe_2O_3) is pointed out as being a more suitable photoanode, when compared to TiO_2, because of its lower band gap (around 2.2 eV) that enables up to 16% conversion efficiency, electrochemical stability, abundance, and relatively low effective cost.[7] Nevertheless, the hematite is also far from being an ideal material for several reasons, such as short hole diffusion length,[19,20] poor oxygen evolution reaction at solid−liquid junction, and unfavorable conduction band position not allowing the water reduction to occur spontaneously, making necessary an application with external potential.[21]

To overcome the hematite limitations, a lot of attention has been dedicated to developing new synthetic routes.[22−26] For example, nanoparticles doping[27−30] and ultrathin undelayer deposited prior to hematite layer[31,32] in order to avoid the high recombination rate and enhance their photocatalytic activity. Still, great improvement has been achieved using the undoped hematite with vertical nanorods oriented onto conducting substrate produced under hydrothermal conditions in a highly acid or basic solution.[33−37] Recently, we have reported an undoped hematite photoanode with great photoelectrochemical performance produced by hydrothermal synthesis in highly acid medium.[36] In that work, the oxygen evolution reaction (OER) at fixed OH^- concentration (1 M NaOH, aqueous electrolyte) was discussed and suggested an intermediary step on classical OER mechanism,[2,3,38−43] showing that the occurrence of OH^- adsorption at hematite surface consequently form an oxy-hydroxide group, playing an important role during water oxidation.[36]

In this current work, we have done an extensively characterization to understand the influence of thermal treatments on as-prepared samples synthesized under hydrothermal conditions. Phase evolution from akaganéite (as-prepared sample) to hematite was accompanied by X-ray

Received: July 23, 2012
Accepted: September 19, 2012
Published: September 19, 2012

   dx.doi.org/10.1021/am301425e | ACS Appl. Mater. Interfaces 2012, 4, 5515−5523

absorption near edge structure (XANES) spectra at Brazilian Synchrotron Light Laboratory (LNLS, Campinas-SP) at iron K-edge energy. The interface nanostructure/aqueous electrolyte performance was analyzed (at room temperature) by cyclic voltammetry (CV) and linear sweep voltammetry (LSV) results, under dark and illuminated conditions. To further explain and confirm the origin of the intermediate step on OER,[36] electrochemical measurements were conducted using KCl aqueous electrolyte with different OH^- content.

EXPERIMENTAL SECTION

Sample Preparation. Our strategy to prepare highly oriented α-Fe_2O_3 nanorod arrays onto a conductor substrate was previously discussed and detailed by elsewhere.[36] This synthetic process was based on the Purpose Built Material (PBM) route that basically consists on a 95 mL aqueous solution (distilled water with resistivity greater than 15 MΩ cm) containing 0.15 mol L^{-1} ferric chloride (Mallinckrodt - $FeCl_3{\cdot}6H_2O$) and 1 mol L^{-1} sodium nitrate (Synth - $NaNO_3$) at pH 1.5 (by Synth - HCl). This solution was poured into an autoclavable bottle containing a polycrystalline conductor fluorine-doped tin oxide (FTO) glass substrate (Flexitec, R_Ω = 10−15 Ω cm^{-1}) vertically held and partially immerse in the solution. The bottle was placed in a regular laboratory oven and subjected to a constant temperature (100 °C) for 6 h in air. After the growth process, the substrates were washed in distilled water in an ultrasonic bath to remove any extra residual salts and allowed to dry in air at room temperature. After this procedure, the substrates covered with iron oxide were taken to a thermal treatment of different temperatures (150, 250, 390, 450, and 530 °C) in a laboratory oven for 1 h and a heating/cooling rate of 1 °C/min. Table 1 summarizes all samples fabricated by this process and analyzed during the current work.

Table 1. Experimental Conditions Used for the Preparation of All Samples

sample preparation	sample code
FTO covered by iron oxide layer after hydrothermal treatment for 6 h.	FeOOH
FeOOH sample thermal treated at 150 °C for 1 h.	S150
FeOOH sample thermal treated at 250 °C for 1 h.	S250
FeOOH sample thermal treated at 390 °C for 1 h.	S390
FeOOH sample thermal treated at 450 °C for 1 h.	S450
FeOOH sample thermal treated at 530 °C for 1 h.	S530

Characterization. The crystalline phases of iron oxide films (before and after the heat treatment) were identified by XRD (Rigaku D-Max 200, using Cu Kα radiation) with the rotary anode operating at 150 kV and 40 mA) in the 2θ range from 10 to 80° with a step scan of 0.02°, 12 s per step. X-ray absorption near edge structure (XANES) measurements were conducted at the XAFS2 beamline of the Brazilian Synchrotron Light Laboratory (LNLS, Campinas, Brazil) in the 7100−7160 eV range with 0.2 eV steps. The spectra were collected at the Fe−K edge using transmission mode for powder samples and fluorescence mode for film samples. The optical characterization was performed by a Varian Cary 50 Conc UV−vis spectrophotometer. FE-SEM top-view and cross-section images of the samples were obtained by Zeiss Supra 35 microscope. The electrochemical measurements were carried out by scanning potentiostat (Potentiostat/Galvanostat μAutolab III with Fra) by cyclic voltammetry mode at a scan rate from 5 to 50 mV/s and range from −0.8 to 0.8 V under dark and illuminated conditions in a standard three-electrode cell using the FTO-iron oxide samples as working electrodes (1.0 cm^2 isolated area), Ag/AgCl in a KCl-saturated solution as the reference electrode and platinum foil as the counter electrode. NaOH (Sigma-Aldrich pro-analysis) and KCl (Vetec) in high-purity water were used for electrolyte preparation. The cell was purged with nitrogen before analyzing to remove the inner oxygen. For electrochemical analyses at illuminated conditions the sunlight was simulated using a 450 W xenon lamp (Osram, ozone free) and an AM 1.5 filter. The light intensity was set to 100 mW cm^{-2}.

RESULTS AND DISCUSSION

Vertically oriented nanorod films prepared by hydrothermal process grew directly on the FTO conductor substrate in hydrated iron oxide phase (akaganéite) as identified using JCPDS 34−1266 catalog and X-ray diffraction curves. The films obtained from the thermal treatment process showed different colors depending on the temperature. The Figure 1 illustrates each stage from the clean substrate to the as-prepared samples before and after additional thermal treatment. A yellow color indicates the presence of hydrated phase and red indicates the dehydrated iron oxide phase, hematite.

From the XRD curves, the as-prepared sample (yellow color) was identified as being an oxyhydroxide phase of iron oxide, akaganéite or β-FeOOH (Figure 1b). After additional thermal treatment, we observe a color change from yellow to red, what characterizes a phase transition to hematite (Figure 1d−g) caused by the structural water elimination or dehydratation. Figure 1a in the Supporting Information illustrates the X-ray diffraction curve for as-prepared samples thermal treated at 390

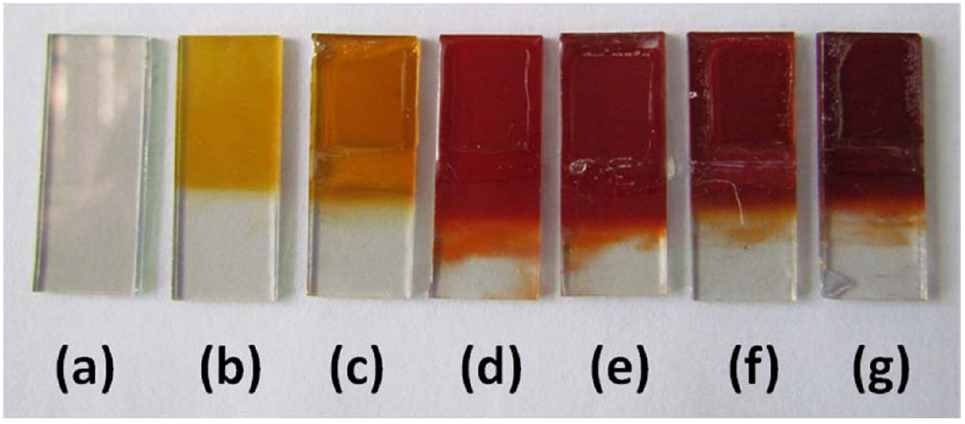

Figure 1. Picture illustrates the stages of the electrodes fabrication process and the samples thermal treated at different temperatures. (a) FTO before hydrothermal process, (b) FTO covered by the iron oxide film after hydrothermal process without thermal treatment, (c) samples after 150, (d) 250, (e) 390, (f) 450, and (g) 530 °C thermal treatment.

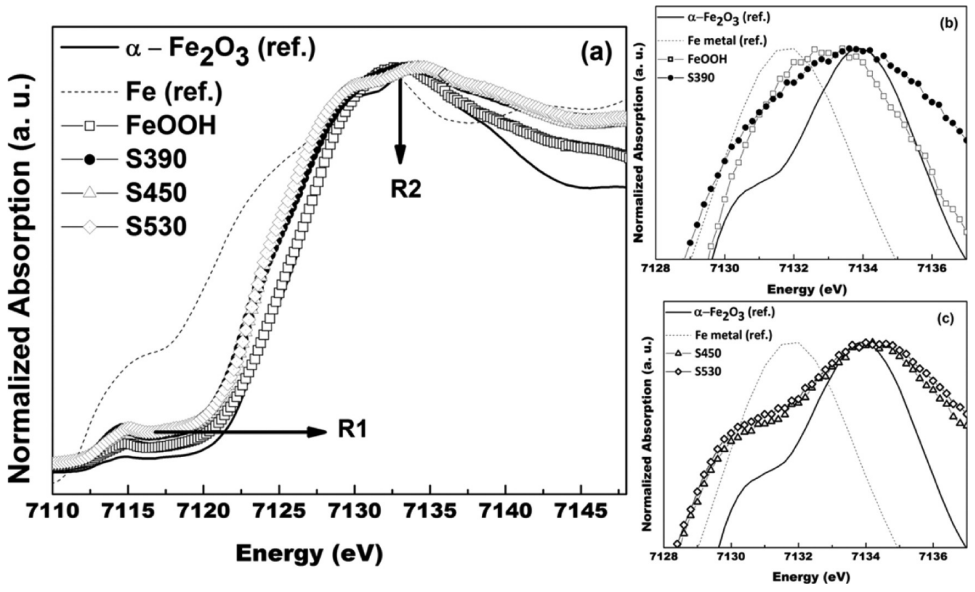

Figure 2. XANES at the Fe−K edge of the as-prepared sample and samples heat treated at different temperatures (fluorescence mode). To better discussion, the entire spectra were divided in R1 and R2, regions at low and high energy respectively. (a) Entire spectra for all samples; (b) R2 region of the spectra for reference, FeOOH and S390 samples; (c) R2 region (for S450, S530 and references samples. The Fe metal and α-Fe_2O_3 (hematite powder) spectra were included for comparison (transmission mode).

°C for 1 h with only indexed peaks referent to hematite phase (JCPDS catalog, 33−0664) and tin oxide (F:SnO_2, FTO) from the substrate. An important requirement to produce promising photoactive hematite film is the preferential orientation of the crystal planes, i.e., the preferential orientation is known to direct influence the conductivity of materials, such as hematite, with strong anisotropic carrier-transport properties. Photoactive hematite film grown in the [110] direction (basal plane (001) of hematite) presents conductivity 4 orders of magnitude higher when measured in perpendicular direction.[44−46] In the present work, the XRD curves for prepared samples exhibited preferential orientation of the nanorod at [110] direction. In previous work, this preferential orientation was attributed as the main reason to enhance the electron transport through the nanostructured films, and as consequence, presents a good photoelectrochemical performance.[36] To better illustrate the preferential orientation obtained, we compare in Figure 1b in the Supporting Information (important portion of the XRD, from 30 to 40° in 2θ) the sample thermally treated at 390 °C for 1 h with hematite nanorod powder. In fact, the XRD data, as expected, exhibits a preferential orientation in [110] direction by all samples, what lead us to suggest that the substrate is responsible by the nanostructure growth in that direction. It is worth mentioning that this result plays an important role when the hematite is intended to be applied in PEC cells, as recently discussed in the literature.[46]

To investigate the effect of the thermal treatment and confirm the hematite formation from akaganéite phase, X-ray absorption near edge structure (XANES) was carried out. The XANES spectra at the Fe−K edge was normalized for all samples synthesized; for better comparison the Fe and α-Fe_2O_3 (Aldrich, commercial hematite bulk) are included as reference. Figure 2 illustrate the XANES profile for all samples with two distinct regions at low (R1) and high (R2) energy, characteristic behavior found for iron based materials. The first region (R1) in XANES spectra is the (low energy) pre-edge which presents a similar profile and intensity for all samples studied here, except for the Fe metallic reference, which has a much higher pre-edge intensity (Figure 2a). The second region (R2) considered as postedge (high energy) evidence the effect of the thermal treatment on the as-prepared samples in which a shoulder, before a maximum absorption peak, appears at temperatures higher than 400 °C, depicted in detail in Figure 2b and c. In addition, the maximum peak moves to higher energy with increase in temperature of the thermal treatment (from akaganéite to hematite formation, see Figure 2b and c).[47]

On the second region (R2), Figure 2b, the as-prepared sample (β-FeOOH nanorod samples) presents one peak with its maximum at energies between those of metallic Fe and α-Fe_2O_3 reference samples, and it starts to decrease at a lower energy than that of α-Fe_2O_3 reference sample. Furthermore, there is no defined shoulder in the spectrum in comparison with the α-Fe_2O_3 reference. Usually, this single peak observed in the XANES spectra around 7140 eV is attributed to dipole-allowed 1s to 4p electron transition, indicating the presence of Fe(III).[47−55] Similarly, it was found in the literature that the intensity of the 1s to 4p transition was proportional to the population of Fe(III) of the β-FeOOH nanorod, in which the oxygen might be the major atom coordinated to the central Fe atoms in that structure.[48] For the sample thermal treated at 390 °C the presence of a slight shoulder can be observed and the spectrum decreases at energy similar to that α-Fe_2O_3 synthesized here, see Figure 2b. Samples thermally treated at 450 and 530 °C are very similar, presenting a well-defined shoulder (around 7130 eV), and the peak of maximum energy at 7134 eV similar to the α-Fe_2O_3 reference, Figure 2b.

On the first region (R1), the pre-edge, it can be observed a peak at 7115 eV for all samples synthesized with a slight change to higher intensities when increasing the temperature of thermal treatment. The same temperature effects on pre-edge intensity were already observed by many authors in the literature during oxyhydroxyde dehydratation to form hematite, including nanosized cases, i.e., pre-edge intensities are sensitive to the local coordination geometry of the metal atom. Additionally, the pre-edge is related to quadrupole transition

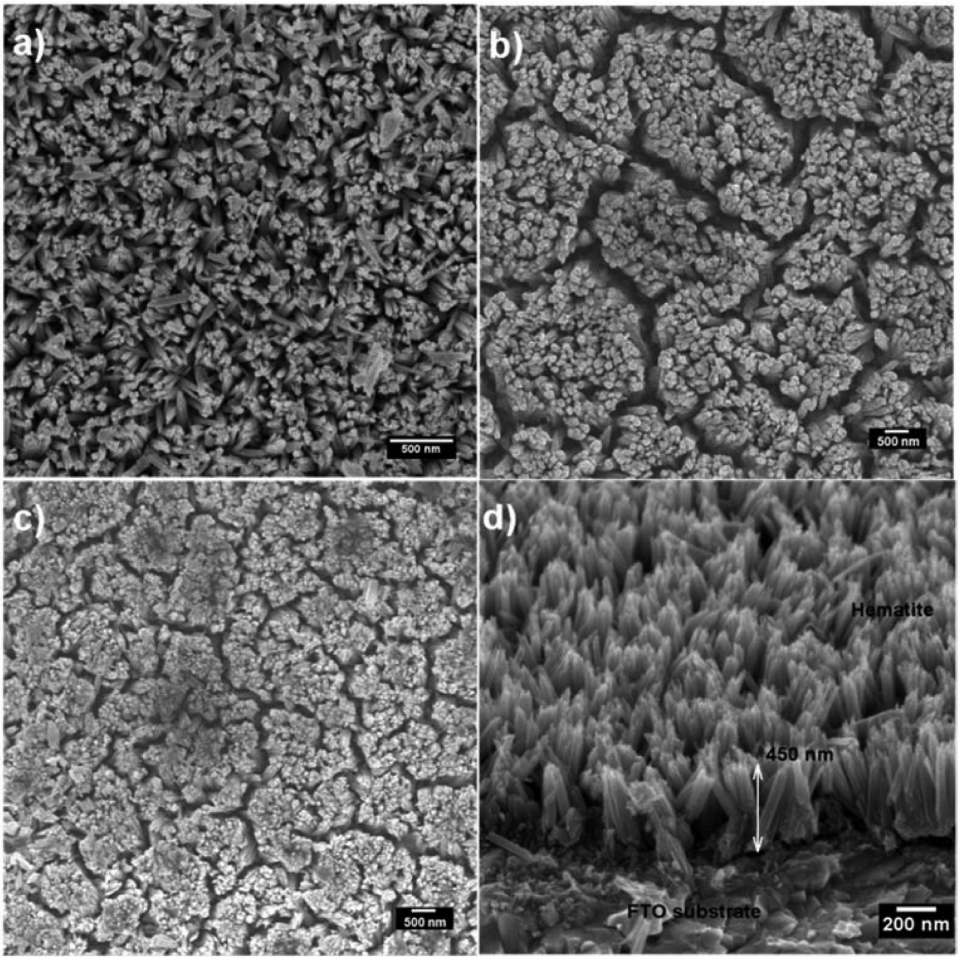

Figure 3. FE-SEM top of view images for undoped nanostructured FTO modified with iron oxide layers: (a) S390, (b) S450, and (c) S530 for 1 h, (d) Cross-section image of the S390 sample. All analyzed samples in the current work were prepared during 6 h by the PBM route on FTO (520 nm thickness).

from 1s to 3d orbital and their peak positions are direct linked to the crystal field splitting of 3d orbital sub-bands.[47−55]

Based on the XANES spectra analysis, we could suggest that the as-prepared sample treated at lower temperature (<400 °C) was not able to completely transform into pure hematite, i.e., comparing with the as-prepared and hematite reference samples a significant contribution coming from the oxyhydroxides phases could be suggested. In addition, from the inset of Figure 2, we clearly confirm that the samples thermal treated at temperatures higher than 400 °C exhibited a profile similar to our hematite reference. The difference in the intensity between synthesized and references samples are probably related to the detection modes used (transmission and fluorescence mode, for powder and films, respectively).

From the FE-SEM images (Figure 3) it is possible to see that the Purpose Built Materials (PBM) route results in a highly orientated material distributed on a large area (1 cm^2). The thin hematite films are composed by vertically oriented nanorods around 400 nm tall with a diameter between 30 and 50 nm. After a 390 °C (Figure 3a) thermal treatment, the electrode shows a very homogeneous distribution of nanorods, however, higher temperature treatments (Figure 3b, c) showed an increase of nanorods agglomeration into blocks. This agglomeration could compromise the solid/liquid surface reaction available, for instance, hindering the transport of holes from the semiconductor to the electrolyte.

The capacity to absorb high portion of the solar irradiation spectrum is a requirement for any semiconductor to be employed in PEC systems. This means that the main principle of PEC devices is to produce hydrogen and oxygen from promotion of holes and electrons on the semiconductor film/liquid interface by solar light irradiation. Figure 4 shows the absorption spectra for pure FTO substrate and FTO modified with the hematite film (samples illustrated in Figure 1) without and with different thermal treatments. To better illustrate the comparison between pure FTO and the modified samples, the transmittance curve is included as inset in Figure 4. As expected, the transmittance is modified by the iron oxide layer and decreases drastically with the increase of the thermal treatment temperature. The dehydratation of as-prepared sample to form hematite, changing the film color from yellow to red, is responsible for strong reduction on transmittance. Plus, the FTO substrate has very low absorption in the visible range; i.e., it does not significantly participate in the global photocurrent response during application in the PEC cell. The thermal treatments clearly affect the optical properties of the film enhancing the absorption range with maximum absorption varying from 200 up to 570 nm. For the samples as-prepared and thermal treated at 150 °C the maximum absorption observed occurs from 200 up to 440 nm (hydrated iron oxide phase, Figure 1) and abruptly decrease the absorption from 450 to 800 nm (Figure 4). Otherwise, for the samples thermal

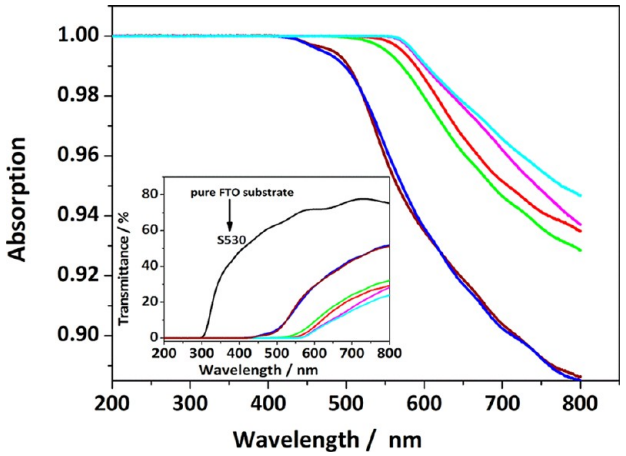

Figure 4. Absorption versus wavelength spectra for FTO substrate modified with hematite obtained from thermal treatment of different temperatures. The inset illustrates the transmittance versus wavelength curves of the samples compared with the pure FTO substrate. The air was used as reference.

treated from 250 to 530 °C, the red color becomes more intense (green to light blue line, Figure 1) and the absorption increases with the thermal treatment temperature. The maximum absorption extends up to 570 nm and then starts to decrease, going to the red region of the spectra. It is known that high light absorption extended to wavelengths higher than 574 nm indicates of existence of sub-bandgap states.[56]

Furthermore, the absorption coefficient α and the band gap E_G are related through the equation $(\alpha h\nu) = A_o(h\nu - E_G)^m$, where $h\nu$ is the photon energy (eV), E_G is the optical band gap energy (eV) and A_o is a constant, and m is equal to 1/2 for a direct allowed and 2 for an indirect forbidden transition. The band gap (E_G) can be calculated from the Tauc plot, $(\alpha h\nu)^{1/m}$ *vs* $h\nu$, by extending a line from the maximum slope of the curve to the *X*-axis in the region of strong absorption.[56−59]

Table 2 summarizes the gap results for all samples fabricated (more details of the gap determination in Figure 2 in the Supporting Information). The values obtained by samples made mostly of hematite (S 450 and S530) present a good agreement with the literature for nanostructured vertically oriented hematite.[36,56] For these samples the thermal treatment seems to affect decreasing the direct bandgap energies and increasing the indirect bandgap energies. Moreover, samples without and thermal treated at lower temperatures, made mostly of akaganéite phase, present higher direct band gaps values and two values of indirect band gap. The higher values (2.32 and 2.16 eV) of indirect band gap are associated with β-FeOOH phase and lower values following the hematite pattern, what agrees with the results obtained by structural analysis, where samples with lower temperatures of thermal treatment are distinguished by a phase mixture of β-FeOOH and α-Fe_2O_3 phases. Blue shifts for these samples, when compared with β-FeOOH bulk bandgap (around 2,13 eV), might be due to quantization effect in the nanorod films and by poor crystallinity, because often the band gap of crystalline material is smaller than that of amorphous materials.[60,61]

Table 2. Calculated Energy Gaps for All Iron Oxide Samples Synthesized by Hydrothermal Process and Thermal Treated at Different Temperatures

sample	direct (eV)	indirect (eV)
FeOOH	2.77 and 2.26	2.32 and 1.79
S150	2.8	2.16 and 1.66
S250	2.33	1.62
S390	2.2	1.7
S450	2.13	1.88
S530	2.13	1.93

The temperature of thermal treatment effect on electrochemical properties of FTO substrate modified with nanorod vertically oriented iron oxide, a detailed study using cyclic voltammetry was performed. The experimental setup used for this measurement was three electrode configuration cells, where the FTO substrate modified with iron oxide layer was used as work electrode, platinum foils as counter electrode and Ag/AgCl as reference. The aqueous solution contains 1 mol L^{-1} of NaOH was the electrolyte. The electrochemical stability was tested cycling all samples synthesized for several times (20 cycles, see the Supporting Information, Figure 3) through a basic solution with a potential window ranging from 0.8 to −0.8 V under dark conditions (Figure 5a). There was no evidence of degradation or dissolution of iron oxide layer in these conditions. From this potential range (Figure 5a) an increase in the current density (J) can be observed comparing pure FTO with iron oxide layers modified FTO (as-prepared and thermal treated samples). On the other hand, unexpected results illustrated in Figure 5 were obtained, in which the films treated at lower temperatures (S150 and S250) exhibited an electrical current density higher than presented for samples thermal treated at higher temperatures (>300 °C). It is common to found better electrocatalytic performance through the highly basic medium (in dark and illuminated condition) for iron oxide layers made of pure hematite crystallographic arrangements. In the current work, contrary results were observed, i.e., the samples with mixed crystallographic arrangement coming from akaganéite and hematite presented higher current densities when compared with the samples with pure hematite arrangement (as pointed out by XANES experiment). In fact, one hypothesis to explain this result could be addressed to the morphology aspect, where samples treated at high temperature (>390 °C) the distance between vertical rods onto substrate are drastically reduced. For instance, top-view illustrated by SEM images of the as-prepared samples (and treated at low temperature) show a very open morphology, in contrast, samples thermal treated at high temperatures present rods agglomeration into nanorod blocks, see Figure 3a−d. To investigate this hypothesis, we performed the electrochemical measurement (for all samples synthesized here) under illuminated conditions using a solar irradiation simulator with AM 1.5 global filters. It is important to mention that the photocatalytic property is commonly observed in iron oxide exclusively with hematite crystallographic arrangement. The better photoelectrochemical response was observed for S390 sample (see inset in the Supporting Information, Figure 4) and no significant changes in current density was observed for other samples (see the Supporting Information, Figure 4). For pure FTO substrate, as-prepared without and with low temperature of treatment (S150 and S250) no change under illumination was expected, because of its low light absorption and low presence of hematite phase as previous discussed. Pure hematite achieved at higher temperatures of treatment (as showed by XANES results) presented the worst photoelectrochemical response, i.e., no changes in the current density

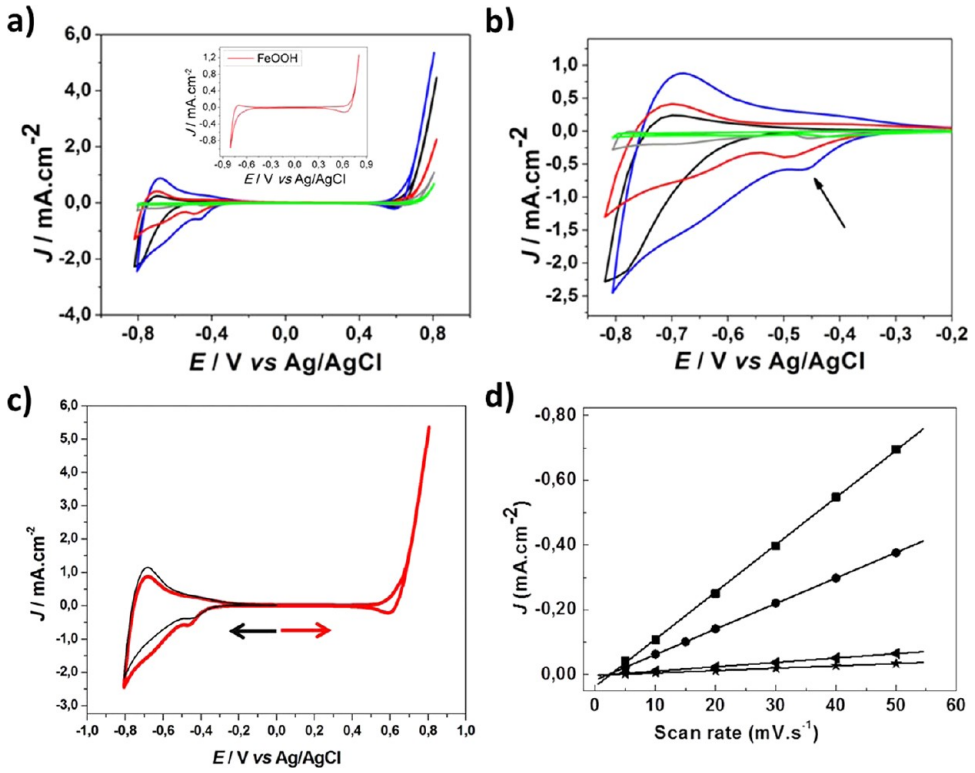

Figure 5. Cyclic voltammograms under dark conditions at pH 13 (NaOH) of the, (a) FTO electrode and thermal treated FTO iron oxide layers represented by: S150-black, S250-blue, S390-red, S450-gray, and S530-green lines. Inset: the as-prepared sample (β-FeOOH) for better comparison. (b) Zoom at the negative potential of a. (c) FTO-iron oxide electrode treated at 250 °C (black line) measured at a negative potential and at a positive potential sequenced by negative potential (red line). All measurements were performed at 50 mV s^{-1} (23 °C ± 0.1 °C), and (d) Linear fitting of current density (J) versus scan rate of FTO-iron oxide samples at pH 13, (■) S250, (●) S390, (◀) S450, and (*) S530. Electrolyte: NaOH 0.1 mol L^{-1}.

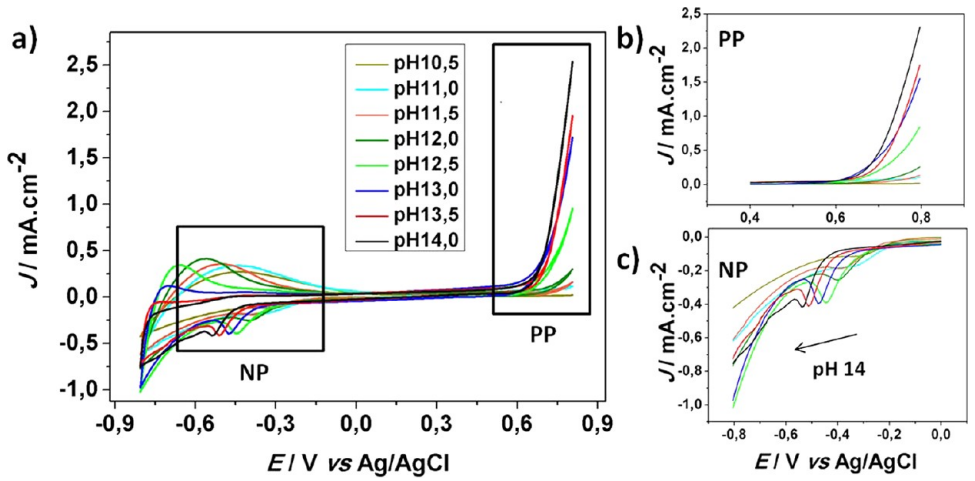

Figure 6. (a) Cyclic voltammograms under dark conditions of the FTO-iron oxide electrode thermal treated at 390 °C at pH variation. (b) Zoom at the positive potential (PP). (c) Zoom at the irreversible reduction peak at negative potential (NP) All measurements were performed at 50 mV s^{-1} (23 °C ± 0.1 °C). Electrolyte: aqueous solution of KCl (0.1 mol L^{-1}) and variation of NaOH (pH from 10.5 to 14.0).

was obtained. Based on this result we believe that the S390 sample showed an enhancement in the current density (0.9 mA cm^{-2} at 0.39 V) related to the favorable morphology allied a significant portion of hematite obtained from the β-FeOOH dehydratation. From this discussion, we suggest that to better extract high photoelectrochemical response, consequently high hydrogen production rate, a carefully control of the iron oxide nanorods distance needs to be importantly considerate. The pure hematite phase was not sufficient to overcome the problems with the morphology and develop a remarkable photoanode; many others requirements need to be satisfied as extensively shown in the literature.[1−7,13−30]

Moreover, from the cyclic voltammogram curves it is clearly observable an irreversible reduction peak at around −0.5 V (Figure 5b). The peak is better defined by higher temperatures of treatments; the 250 °C treated sample, which shows the higher current density (dark condition) results, also has the biggest reduction peak. In a recent study conducted by

Carvalho,[36] it was suggested that this electrochemical process originates from the adsorption of OH^- groups at the surface of the nanorods. In that work, this peak was considered responsible for the oxygen molecular evolution because of consumption of OH^- during the anodic scan. It is worth mentioning that this adsorption process appears only when the electrochemistry measurement is first followed by a positive potential pathway, otherwise, this process does not appear (as depicted in Figure 5c).[36] The Figure 5d illustrates a linear behavior between different values of velocity of scan and the maximum density current of the irreversible reduction peaks, what indicates that this reaction is limited by charge transfer. Samples without and thermal treated under low temperatures (S150) are not considered in this analysis because of the peak absence at negative potentials. Higher thermal treatment promotes the samples from akaganéite (of β-FeOOH) to pure hematite (α-Fe_2O_3); however, it seems to affect the current density of the peak (at negative and positive potential) decreasing electrocatalytic performance compared with samples thermal treated at S250 and S390. Indeed, as viewed at the morphology discussion, higher temperatures induced an agglomeration of nanorods into blocks, which could reduce the surface available to reaction, and/or nanosize defects, created by the water elimination during the phase transition. It is general observed that this parameters act directly as obstacles for the electron−hole mobility and benefit the electron−hole recombination.[26]

It is worth mentioning that the presence of the irreversible peak at negative potential for vertically oriented nanorods onto FTO substrate was suggested to be strong dependent on OH^- concentration (aqueous electrolyte).[36] To gain further information about the origin of this process an electrochemical characterization was conducted in dark conditions with electrolyte containing different OH^- concentration. Figure 6a illustrate the current densities generated by the sample S390 performed from 0.8 to −0.8 V in KCl 0.1 mol. L^{-1} electrolyte with different NaOH content. For this discussion, the voltammogram curves were divided in two regions: positive potential (PP) and negative potential (NP), Figure 6b and c.

Figure 6b exhibit the behavior of PP region in function of different OH^- content for S390 sample and a gradual reduction on electrocatalytic activity is observed from high to low pH solution. This electrocatalytic activity shift to low positive potential with increase of OH^-concentration is one of most important requirement for semiconductor to be useful in PEC cell to split water producing H_2. Indeed, the electrocatalytic activity seems to be strong related to the consumption of OH^- adsorbed on hematite surface (at NP), i.e., the highest electrocatalytic performance is dependent on the OH^- content adsorbed, as exhibited in Figure 6.

The negative potential region (NP) is marked by an irreversible reduction peak, as already mentioned in the literature for iron oxide film,[36] and attributed to adsorption of hydroxyl species at the hematite electrode surface (depicted in Figure 6c). For further understanding, all samples synthesized here were measured at several solution pH and the same dependence with OH^- content for positive and negative potential were observed, see the Supporting Information, Figure 4. Moreover, the electrochemical performance at different pH comparing all samples are depicted in the Supporting Information, Figure 4, which pointed out that the S250 sample, in agreement with previous experiments discussed here, presents a better electrocatalytic performance at pH range studied. Once again, we may suggest that the high temperature of thermal treatment could be reducing the surface area available to react with the electrolyte and/or adsorb any kind of species.

A general and extensively discussion has been addressed in the literature to the presence of this peak at negative potential mainly for TiO_2 base nanostructured materials.[62−76] Usually, this peak is observed at more negative potential (from −0.8 to −0.6 V) compared with that peak discussed here, and are attributed to a charge accumulation basically explained by two different mechanisms. The first one is based on standard dielectric capacitor where their capacitance is linked to a spatial charge separation, usually comparable to capacitance present at the Schottky barriers and Helmholtz layers. The second is named chemical capacitance, extensively studied and attributed as significant to explain that behavior for ion intercalation materials, nanostructured semiconductors and organic conductors.[62,77−79] The chemical capacitance has been related to increase the specie number on bulk material, where conduction current is responsible for charging the capacitor.[77,79] On the basis of cyclic voltammetry curves measured in function of OH^- content in the electrolyte we suggest that the OH^- groups are responsible for appearance of this peak at negative potential, and also the shift to lower positive potential of the water oxidation process. As consequence for those assumptions, Nernstian H^+/OH^- equilibrium effects are suggested because of their strong dependence with the OH^- concentration, similarly to the equilibrium reported to nanostructured TiO_2 films.[70,71] Moreover, this chemical interaction between OH^- species and iron oxide surface seems to play an important step on the water oxidation mechanism, as already discussed. This intermediate step attributed a formation of oxyhydroxide on the iron oxide surface preceding the oxygen molecular evolution is not inconsistent with thermodynamical parameters extracted from the Pourbaix diagram for bulk material. There is a vast number of works in the literature that related this peak at NP with the formation of different stable species formation at iron oxide surface during water oxidation process.[80−82]

More recently, a detailed electrochemical and photoeletrochemical investigation to understand the hematite/liquid interface and their implication in how to overcome the overpotential required to oxidize water, was addressed by Klahr and co-workers. In that work the authors suggested that the formation of species on the iron oxide surface as being an intrinsic part of the biomolecular mechanism of water oxidation. Nevertheless, they believe that the real factor that limits the efficient water oxidation at low potential is the surface state recombination process, which is not observed in called ideal behavior, when the hematite was investigated at high positive potential using different environment.[83] However, in our case, the presence of peak at NP related to stable species formation, also observed by other in the literature,[82] are confirmed by the experiments showed by Klahr, where the difference in the potential between two surface states was observed.

CONCLUSION

In summary, the thermal treatment revealed to play an important role in the fundamental properties of vertical oriented iron oxide nanorods layer deposited onto conductor substrate, a promising candidate as photoanode to be used in a PEC cell. The structural evolution promoted by sinterization process was monitored by X-ray diffraction and XANES

spectra, and the as-prepared samples was identified as having a crystallographic arrangement of hydrated phase of the iron (accordingly with JCPDS catalog, β -FeOOH, akaganéite). From different temperature of treatment and as consequence of structural water elimination the β -FeOOH becomes a pure α-Fe_2O_3 (hematite phase) at temperature above 450 °C as verified by XANES results. SEM images illustrate the formation of rods vertically oriented to the substrate and distributed along of the 1 cm^2 of area forming a mesopouros arrangement. However, at higher temperatures of thermal treatment the morphology becomes more compact and presents a less open surface. The preferential orientation of the rods was identified by XRD diffraction data as being (001) basal plane of hematite, perpendicular to the substrate, for samples heat treated at temperature higher than 390 °C. This orientation is known to be a highly conductive for hematite nanostructures, an important requirement for photoelectrochemical applications. The light absorption increase with temperature of treatment and a maximum absorption was observed from 200 to 600 nm. In addition, the band gap was estimated for all samples and the slight reduction is observed with increase of the temperature. Both results are also interesting for using the hematite as a photoanode, i.e., high light absorption at visible range and favorable band gap is required to have an efficient performance to split water. Moreover, the temperature was able to transform the as prepared sample into pure hematite material, however, the consequence caused in the morphology drastically affected their performance during electrochemical and photoelectrochemical experiments. In addition, the electrochemical measurement performed with electrolyte contained different pH shown that OH^- groups play an important role shifting the water oxidation to lower positive potential. As a consequence, an intermediate step that considers the first formation of oxyhydroxide species at the iron oxide surface preceding the water oxidation mechanism seems to be reasonable, as first mentioned by Carvalho.[36] Finally, we found that many physical chemical properties must be in harmony in order to design a promising material to efficiently perform the water splitting using solar light energy. More experiments to confirm and better understand the water mechanism oxidation are underway in our laboratory.

■ ASSOCIATED CONTENT

Ⓢ Supporting Information

More details about the X-ray diffraction data, optical band gap calculation, electrochemical curves at different pH and photoelectrochemical measured under dark and illuminated conditions. This material is available free of charge via the Internet at http://pubs.acs.org.

■ AUTHOR INFORMATION

Corresponding Author

*Address: 166 Rua Santa Adélia, 09210-170, Santo André, SP, Brazil. Phone: +55 11 4996 8353. E-mail: fleandro.ufabc@gmail.com and flavio.souza@ufabc.edu.br.

Notes

The authors declare no competing financial interest.

■ ACKNOWLEDGMENTS

We gratefully acknowledge financial support from the Brazilian agencies of FAPESP (Grants 2010/02464-6 and 2011/19390-8), CAPES, CNPq (555855/2010-4), Instituto Nacional em Eletrônica Orgânica (INEO), NanoBioMed Brazil Network (CAPES), and INCTMN.

■ REFERENCES

(1) Grimes, C. A.; Varghese, O. K.; Ranjan, S., Light, water, hydrogen: the solar generation of hydrogen by water photoelectrolysis, Springer Verlag: Berlin, 2008.
(2) Walter, M. G.; Warren, E. L.; McKone, J. R.; Boettcher, S. W.; Mi, Q.; Santori, E. A.; Lewis, N. S. *Chem. Rev.* **2010**, *110*, 6446−6473.
(3) Cook, T. R.; Dogutan, D. K.; Reece, S. Y.; Surendranath, Y.; Teets, T. S.; Nocera, D. G. *Chem. Rev.* **2010**, *110*, 6474−6502.
(4) Katz, M. J.; Riha, S. C.; Jeong, N. C.; Martinson, A. B. F.; Farha, O. K.; Hupp, J. T. *Coord. Chem. Rev.* **2012**, DOI: 10.1016/j.ccr.2012.06.017.
(5) Maeda, K. *J. Photochem. Photobiol. C* **2011**, *12*, 237−268.
(6) Kronawitter, C. X.; Vayssieres, L.; Shen, S.; Guo, L.; Wheeler, D. A.; Zhang, J. Z.; Antounf, B. R.; Mao, S. S. *Energy Environ. Sci.* **2011**, *4*, 3889.
(7) Valdés, A.; Brillet, J.; Gratzel, M.; Gudmundsdóttir, H.; Hansen, H. A.; Jónsson, H.; Klupfel, P.; Kroes, G.; Le Formal, F.; Man, I. C.; Martins, R. S.; Nørskov, J. K.; Rossmeisl, J.; Sivula, K.; Vojvodic, A.; Zach, M. *Phys. Chem. Chem. Phys.* **2012**, *14*, 49−70.
(8) Fujishima, A.; Honda, K. *Nature* **1972**, *238*, 37−38.
(9) Boddy, P. J. *J. Electrochem. Soc.* **1968**, *115*, 199.
(10) Navarro, R. M.; Alvarez-Galvan, M. C.; Villoria de la Mano, J. A.; Al-Zahrani, S. M.; Fierro, J. L. G. *Energy Environ. Sci.* **2010**, *3*, 1865−1882.
(11) Henderson, M. A. *Surf. Sci. Rep.* **2011**, *66*, 185−297.
(12) Osterloh, F. E. *Chem. Mater.* **2008**, *20*, 35−54.
(13) Van de Krol, R.; Liang, Y. Q.; Schoonman, J. *J. Mater. Chem.* **2008**, *18*, 2311−2320.
(14) Alexander, B. D.; Kulesza, P. J.; Rutkowska, L.; Solarska, R.; Augustynski, J. *J. Mater. Chem.* **2008**, *18*, 2298−2303.
(15) Shankar, K.; Basham, J. I.; Allam, N. K.; Varghese, O. K.; Mor, G. K.; Feng, X. J.; Paulose, M.; Seabold, J. A.; Choi, K. S.; Grimes, C. A. *J. Phys. Chem. C* **2009**, *113*, 6327−6359.
(16) Vayssieres, L. On *Solar Hydrogen & Nanotechnology*; John Wiley & Sons: New York, 2009.
(17) Maeda, K.; Domen, K. *J. Phys. Chem. Lett.* **2010**, *1* (18), 2655−2661.
(18) Kamat, P. V. *J. Phys. Chem. C* **2012**, *116* (22), 11849−11851.
(19) Kennedy, J.; Frese, K. *J. Electrochem. Soc.* **1978**, *125*, 709−714.
(20) Balberg, I.; Pinch, H. *J. Magn. Magn. Mater.* **1978**, *7*, 12−15.
(21) Nozik, A. J.; Memming, R. *J. Phys. Chem.* **1996**, *100*, 13061−13078.
(22) Souza, F. L.; Lopes, K. P.; Longo, E; Leite, E. R. *Phys. Chem. Chem. Phys.* **2009**, *11*, 1215−1219.
(23) Souza, F. L.; Lopes, K. P.; Longo, E.; Leite, E. R. *Sol. Energy Mater. Sol. Cells* **2009**, *93*, 362−368.
(24) Gonçalves, R. H.; Lima, B. H. R.; Leite, E. R. *J. Am. Chem. Soc.* **2011**, *133*, 6012−6019.
(25) Sivula, K.; Zboril, R.; Le Formal, F.; Robert, R.; Weidenkaff, A.; Tucek, J.; Frydrych, J.; Gratzel, M. *J. Am. Chem. Soc.* **2010**, *132* (21), 7436−7444.
(26) Brillet, J.; Gratzel, M.; Sivula, K. *Nano Lett.* **2010**, *10*, 4155−4160.
(27) Kay, A.; Cesar, I.; Gratzel, M. *J. Am. Chem. Soc.* **2006**, *128*, 15714.
(28) Cesar, I.; Kay, A.; Martinez, J. A. G.; Gratzel, M. *J. Am. Chem. Soc.* **2006**, *128*, 4582.
(29) Glasscock, J. A.; Barnes, P. R. F.; Plumb, I. C.; Savvides, N. *J. Phys.Chem. C* **2007**, *111*, 16477−16488.
(30) Tilley, S. D.; Cornuz, M.; Sivula, K.; Gratzel, M. *Angew. Chem., Int. Ed.* **2010**, *49*, 6405−6408.
(31) Hisatomi, T.; Brillet, J.; Cornuz, M.; Le Formal, F.; Tetreault, N.; Sivula, K.; Gratzel, M. *Faraday Discuss.* **2012**, *155*, 223−232.
(32) Hisatomi, T.; Dotan, H.; Stefik, M.; Sivula., K.; Rothschild, A.; Gratzel, M.; Mathews, N. *Adv. Mater.* **2012**, *24*, 2699−2702.

(33) Vayssieres, L.; Beermann, N.; Lindquist, S. E.; Hagfeldt, A. *Chem. Mater.* **2001**, *13* (2), 233−235.
(34) Morrish, R.; Rahman, M.; Don MacElroy, J. M.; Wolden, C. A. *ChemSusChem* **2011**, *4*, 474−479.
(35) Bora, D. K.; Braun, A.; Erni, R.; Fortunato, G.; Graule, T.; Constable, E. C. *Chem. Mater.* **2011**, *23* (8), 2051−2061.
(36) Carvalho, V. A. N.; Luz, R. A. S.; Lima, B.; Leite, E. R.; Crespilho, F. N.; Souza, F. L. *J. Power Sources* **2012**, *205*, 525−529.
(37) Ling, Y.; Wang, G.; Reddy, J.; Wang, C.; Zhang, J. Z.; Li, Y. *Angew. Chem., Int. Ed.* **2012**, *51*, 4074−4079.
(38) Bockris, J. O.; Huq, A. *Proc. R. Soc. Lond. A* **1956**, *237*, 277−296.
(39) Zhong, D. K.; Gamelin, D. R. *J. Am. Chem. Soc.* **2010**, *132*, 4202−4207.
(40) Lutterman, D. A.; Surendranath, Y.; Nocera, D. G. *J. Am. Chem. Soc.* **2009**, *131*, 3838−3839.
(41) Kanan, M. W.; Nocera, D. G. *Science* **2008**, *321*, 1072−1075.
(42) Steinmiller, E. M. P.; Choi, K. S. *Proc. Natl. Acad. Sci. U.S.A.* **2009**, *106*, 20633−20636.
(43) Trasatti, S. In *The Electrochemistry of Novel Materials*; VCH Publishers: New York, 1994.
(44) Nakau, T. *Jpn. J. Phys. Soc.* **1960**, *15*, 727.
(45) Benjelloun, D.; Bonnet, J. P.; Doumerc, J. P.; Launay, J. C.; Onillon, M.; Hagenmuller, P. *Mater. Chem. Phys.* **1984**, *10*, 503.
(46) Cornuz, M.; Gratzel, M.; Kevin, S. *Chem. Vap. Deposition* **2010**, *16*, 291−295.
(47) Bora, D. K.; Braun, A.; Erat, S.; Safonova, O.; Graule, T.; Constable, E. C. *Curr. Appl. Phys.* **2012**, *12* (3), 817−825.
(48) Lin, K.; Wang, Z.; Chowdhury, S.; Adhikari, A. K. *Thin Solid Films* **2009**, *517*, 5192−5196.
(49) Chen, L. X.; Liu, T.; Thurnauer, M. C.; Csencsits, R.; Rajh, T. *J. Phys. Chem. B* **2002**, *106*, 8539−8546.
(50) Glatzel, P.; Mirone, A.; Eeckhout, S. G.; Sikora, M. *Phys. Rev. B* **2008**, *77*, 115133.
(51) Grunes, L. A. *Phys. Rev. B* **1982**, *27* (4), 2111−2131.
(52) Canepa, P.; Schofield, E.; Chadwick, A. V.; Alfredsson, M. *Phys. Chem. Chem. Phys.* **2011**, *13*, 12826−12834.
(53) Modrow, H.; Bucher, S.; Rehr, J. J.; Ankudinov, A. L. *Phys. Rev. B* **2003**, *67*, 035123.
(54) Bair, R. A.; Goddard, W. A. *Phys. Rev. B* **1980**, *22*, 2767.
(55) Park, T.; Sambasivan, S.; Fischer, D. A.; Yoon; Misewich, W. J. A.; Wong, S. S. *J. Phys. Chem. C* **2008**, *112*, 10359−10369.
(56) Beermann, N.; Vayssieres, L.; Lindquist, S. E.; Hagfeldt, A. *J. Electrochem. Soc.* **2000**, *147* (7), 2456−2461.
(57) Mohapatra, S. K.; Misra, M.; Mahajan, V. K.; Raja, K. S. *J. Phys. Chem. C* **2007**, *111*, 8677−8685.
(58) Cole, B.; Marsen, B.; Miller, E.; Yan, Y.; To, B.; Jones, K.; Al-Jassim, M. *J. Phys. Chem. C* **2008**, *112*, 5213−5220.
(59) Miller, E. L.; Paluselli, D.; Marsen, B.; Rocheleau, R. E. *Thin Solid Films* **2004**, *466*, 307−313.
(60) Mor, G. K.; Varghese, O. K.; Paulose, M.; Shankar, K.; Grimes, C. A. *Sol. Energy Mater. Sol. Cells* **2006**, *90*, 2011−2075.
(61) Dghoughi, L.; Elidrissi, B.; Bernède, C.; Addou, M.; Lamrani, M. A.; Regragui, M.; Erguig, H. *Appl. Surf. Sci.* **2006**, *253*, 1823−1829.
(62) Leng, W. H.; Zhang, Z.; Zhang, J. Q.; Cao, C. N. *J. Phys. Chem. B* **2005**, *109* (31), 15008−15023.
(63) Van de Krol, R.; Gratzel, M. *Photoelectrochemical Hydrogen Production*; Springer Verlag: Berlin, 2012, 102.
(64) Bisquert, J.; Fabregat-Santiago, F.; Mora-Seró, I.; Garcia-Belmonte, G.; Barea, E. M.; Palomares, E. *Inorg. Chim. Acta* **2008**, *361*, 684−698.
(65) Cummings, C. Y.; Bonné, M. J.; Edler, K. J.; Helton, M.; Mckee, A.; Marken, F. *Electrochem. Commun.* **2008**, *10* (11), 1773−1776.
(66) Bora, D. K.; Braun, A.; Erat, S.; Ariffin, A. K.; Romy, L.; Sivula, K.; Gratzel, M.; Graule, T.; Constable, E. *J. Phys. Chem. C* **2011**, 5619−5625.
(67) Klahr, B.; Gimenez, S.; Fabregat-Santiago, F.; Hamann, T.; Bisquert, J. *J. Am. Chem. Soc.* **2012**, *134* (9), 4294−4302.
(68) Drissi, S. H.; Abdelmoula, R. M.; Génin, J. M. R. *Corros. Sci.* **1995**, *37* (12), 2025−2041.
(69) Berverskog, B.; Puigdomenech, I. *Corros. Sci.* **1996**, *38*, 2121−2135.
(70) Levine, S.; Smith, A. L. *Discuss. Faraday Soc.* **1971**, *52*, 290−301.
(71) Healy, T. W.; White, L. R. *Adv. Colloid Interface Sci.* **1978**, *9*, 303−345.
(72) Klahr, B. M.; Hamann, T. W. *J. Phys. Chem. C* **2011**, *115*, 8393−8399.
(73) McGregor, K. G.; Calvin, M.; Otvos, J. W. *J. Appl. Phys.* **1979**, *50* (1), 369−373.
(74) Kennedy, J. H.; Frese, K. W. *J. Electrochem. Soc.* **1978**, *125* (5), 723−726.
(75) Launay, J. C.; Horowitz, G. *J. Cryst. Growth* **1982**, *57* (1), 118−124.
(76) Anderman, M.; Kennedy, J. H. *J. Electrochem. Soc.* **1984**, *131* (1), 21−26.
(77) Randriamahazaka, H.; Fabregat-Santiago, F.; Zaban, A.; García-Canãdas, J.; Garcia-Belmonte, G.; Bisquert, J. *Phys. Chem. Chem. Phys.* **2006**, *8*, 1827.
(78) Jamnik, J.; Maier, J. *Phys. Chem. Chem. Phys.* **2001**, *3*, 1668.
(79) Bisquert, J.; Garcia-Belmonte, G.; García-Canãdas, J. *J. Chem. Phys.* **2004**, *120*, 6726.
(80) Dau, H.; Limberg, C.; Reier, T.; Risch, M.; Roggan, S.; Strasser, P. *ChemCatChem* **2010**, *2*, 724.
(81) Conway, B. E.; Tilak, B. V. *Adv. Catal.*; Academic Press: New York, 1992; Vol. *38*, p 1.
(82) Trainor, T. P.; Chaka, A. M.; Eng, P. J.; Newville, M.; Waychunas, G. A.; Catalano, J. G.; Brown, G. E., Jr. *Surf. Sci.* **2004**, *573*, 204.
(83) Klahr, B.; Gimenez, S.; Fabregat-Santiago, F.; Bisquert, J.; Hamann, T. W. *Energy Environ. Sci.* **2012**, *5*, 7626.